



CFFormer: Cross CNN-Transformer Channel Attention and Spatial Feature Fusion for Improved Segmentation of Low Quality Medical Images

Jiaxuan Li^{a,1}, Qing Xu^{a,1}, Xiangjian He^{a,*}, Ziyu Liu^{a, b, d}, Daokun Zhang^{a,*}, Ruili Wang^c, Rong Qu^d, Guoping Qiu^a

^aSchool of Computer Science, University of Nottingham Ningbo China, 199 Taikang East Road, Ningbo, Zhejiang, 315100, China

^bShenzhen Institute of Advanced Technology, Chinese Academy of Sciences, China, Shenzhen, Guangdong, 518055, China

^cSchool of Mathematical and Computational Sciences, Massey University, Auckland, New Zealand

^dUniversity of Nottingham, United Kingdom, University Park, Nottingham, NG7 2RD, United Kingdom

ARTICLE INFO

Article history:

Keywords:

Medical Image Segmentation
Image Segmentation
Deep Learning
Hybrid CNN-Transformer Model

ABSTRACT

Hybrid CNN-Transformer models are designed to combine the advantages of Convolutional Neural Networks (CNNs) and Transformers to efficiently model both local information and long-range dependencies. However, most research tends to focus on integrating the spatial features of CNNs and Transformers, while overlooking the critical importance of channel features. This is particularly significant for model performance in low-quality medical image segmentation. Effective channel feature extraction can significantly enhance the model's ability to capture contextual information and improve its representation capabilities. To address this issue, we propose a hybrid CNN-Transformer model, CFFormer, and introduce two modules: the Cross Feature Channel Attention (CFCA) module and the X-Spatial Feature Fusion (XFF) module. The model incorporates dual encoders, with the CNN encoder focusing on capturing local features and the Transformer encoder modeling global features. The CFCA module filters and facilitates interactions between the channel features from the two encoders, while the XFF module effectively reduces the significant semantic information differences in spatial features, enabling a smooth and cohesive spatial feature fusion. We evaluate our model across eight datasets covering five modalities to test its generalization capability. Experimental results demonstrate that our model outperforms current state-of-the-art (SOTA) methods, with particularly superior performance on datasets characterized by blurry boundaries and low contrast.

© 2025 Elsevier B. V. All rights reserved.

1. Introduction

In modern medicine, medical image segmentation plays a crucial role as an effective data processing method that efficiently identifies abnormal regions. Over the past decades, deep learning-based semantic segmentation techniques have

garnered significant attention from researchers due to their higher efficiency compared to manual annotation. Essentially, semantic segmentation involves classifying pixel values, which enables pixel-level annotation of complex pathological regions in medical images, such as brain tumors, melanomas, and various cancerous areas (Azad et al., 2024; Asgari Taghanaki et al., 2021).

Deep convolutional neural network-based semantic segmentation models have been widely applied to various vision tasks, with U-shaped architectures being particularly popular in the medical field. These models comprise an encoder, which cap-

*Corresponding authors:

e-mail: sean.he@nottingham.edu.cn (Xiangjian He),

daokun.zhang@nottingham.edu.cn (Daokun Zhang)

¹Jiaxuan Li and Qing Xu contributed equally to this work

tures both semantic and contextual information through consecutive convolutional layers and down-sampling, and a decoder, which reconstructs the output mask by progressively up-sampling (Zhou et al., 2019). While deeper convolutional layers and increased down-sampling expand the receptive field, they can result in a loss of contextual information. U-shaped models mitigate this issue by employing skip connections to recover lost context. However, these models still face challenges with limited receptive fields and difficulties in modeling long-range dependencies due to the inherent constraints of convolutional layers (Yuan et al., 2023; Heidari et al., 2023).

Vision Transformers (ViTs) enhance the receptive field by splitting images into patches and modeling relationships between them. However, ViTs are limited in capturing low-level features, as patch-based processing hinders the model's ability to effectively represent feature relationships within individual patches (Heidari et al., 2023).

To combine the strengths of both U-shaped CNN architectures and Transformers, we propose a novel U-shaped hybrid CNN-Transformer model named CFFormer, which embeds two key modules into the encoder layers: a low-parameter Cross Feature Channel Attention (CFCA) Module that efficiently explores channel relationship between CNN and Transformer feature maps, and an X-Spatial Feature Fusion (XFF) Module that effectively fuses feature maps in the spatial domain and eliminates the significant differences in spatial features.

Compared to previous hybrid models, our approach places greater emphasis on the channel attention between the CNN and Transformer encoders. The proposed CFCA module captures attention while projecting channel attention onto each respective feature map, facilitating information exchange between the two encoders. Additionally, the XFF module effectively fuses spatial features, enabling the skip connection feature maps to incorporate both the local information captured by the CNN and the global information captured by the Transformer. To demonstrate the excellent performance of our model, we test it on 8 datasets: BUSI (Al-Dhabyani et al., 2020), Dataset B (Yap et al., 2017), ISIC2016 (Gutman et al., 2016), PH2 (Mendonça et al., 2013), Kvasir Seg (Jha et al., 2020), CVC-ClinicDB (Jha et al., 2019), Synapse multi-organ segmentation dataset (Landman et al., 2015), and Brain-MRI (Buda et al., 2019). These datasets encompass five modalities: Ultrasound Imaging (US), Dermoscopic Imaging, Computed Tomography (CT), Colonoscopy, and Magnetic Resonance Imaging (MRI). Extensive experimental results indicate that our model outperforms current state-of-the-art (SOTA) models across different modalities. Our model presents three-fold contributions compared to state-of-the-art (SOTA) models:

- The proposed Cross Feature Channel Attention (CFCA) module facilitates selective interaction between two feature maps within the encoder layers, effectively addressing the respective shortcomings of CNN models and Transformers in capturing both local and global features.
- The X-Spatial Feature Fusion (XFF) module effectively mitigates the substantial differences, including semantic information discrepancies and contextual information, be-

tween the feature maps of CNNs and Transformers within the encoder layers, thereby enhancing the model's ability to perform spatial feature fusion.

- Our model surpasses state-of-the-art (SOTA) methods on eight datasets with five modalities, and we provide the code to enable further exploration in medical image segmentation.

2. Related Work

Three streams of deep neural network models have been developed to do medical image segmentation, i.e., Convolutional neural networks (CNNs), Transformers and Hybrid CNN-Transformer models. CNNs have limited ability to capture long-range dependencies, which hinders their capacity to fully exploit the semantic information within images (Yao et al., 2024). Transformers enhance the model's global receptive field by modeling patches, but they lack the ability to capture local features (Han et al., 2022). As a result, Hybrid CNN-Transformer models have gained significant attention for combining the strengths of both CNNs and transformers to improve segmentation performance.

2.1. U-shaped CNN Architectures

U-shaped architectures are particularly effective at capturing local information due to their symmetrical encoder-decoder structure, and the skip connections help restore some of the information lost during the downsampling process in the encoder (Zhan et al., 2024). DCSAU-Net, a variant of the U-shaped model, integrates Primary Feature Conservation (PFC) and the Compact Split-Attention (CSA) block. This design results in a deeper and more efficient architecture, enabling the network to effectively capture both low-level and high-level semantic information (Xu et al., 2023). Although DCSAU-Net demonstrates strong performance in semantic information extraction, it still exhibits certain limitations in global information extraction, primarily relying on the large kernel convolutions of the PFC. HDA-ResUNet introduces a channel attention module inspired by the concept of self-attention, which models the dependencies between channels. Additionally, it employs a hybrid dilated attention convolutional layer to fuse information from different receptive field sizes (Wang et al., 2021). Despite modeling channel attention in feature maps to enhance performance and extracting global features from high-level representations, HDA-ResNet cannot fully capture all global features. Furthermore, due to the inherent limitations of convolutional layers, it struggles to effectively model long-range dependencies in feature maps and remains constrained by a limited receptive field.

2.2. Transformer Architectures

Transformers are widely utilized in natural language processing (NLP). Remarkably, BERT, a pre-trained model composed entirely of Transformer encoders, achieves state-of-the-art (SOTA) performance across 11 NLP tasks (Devlin, 2018). Similarly, GPT-3 (Generative Pre-trained Transformer) (Brown, 2020), a model consisting solely of Transformer decoders,

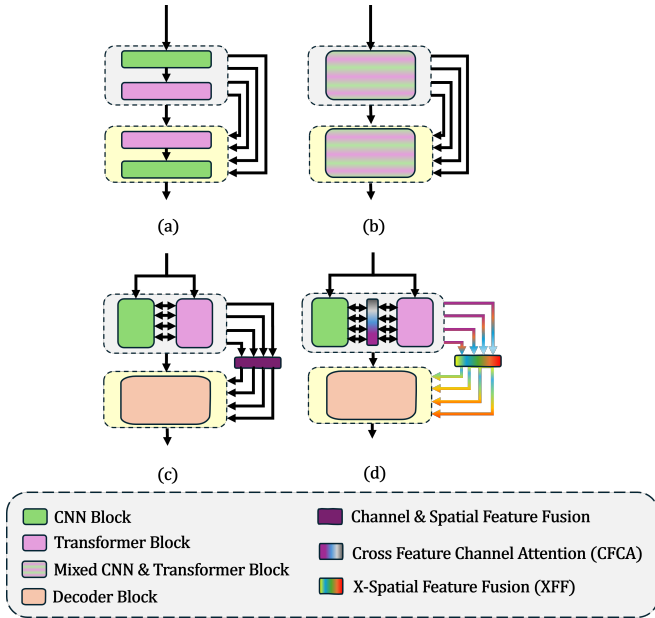


Fig. 1: Four types of CNN-Transformer architectures. (a). Transformers applied in High-level features. (b). Mixture of CNN and transformer for each layer. (c). Feature fusion for dual-encoders CNN-Transformer architecture. (d). CFFormer Architecture.

demonstrates remarkable performance in various downstream NLP tasks. This success prompts researchers to investigate the methods of Transformers in computer vision tasks. Vision Transformer (ViT) is one such successful model, which preserves the core Transformer architecture but employs patch embedding and absolute positional encoding to partition images into patches that serve as tokens for the model to process (Dosovitskiy, 2020). The introduction of the Swin Transformer addresses the limitation in capturing local information by replacing the standard multi-head self-attention (MSA) with window-based multi-head self-attention (W-MSA/SW-MSA) (Liu et al., 2021). By integrating the attention mechanism within sliding windows, the Swin Transformer can effectively capture global information at multiple scales while enhancing its ability to learn local features. Although Transformers are proficient at modeling long-range dependencies, their ability to capture fine-grained local information remains limited (Han et al., 2022).

2.3. Hybrid CNN-Transformer Architectures

There is a strong emphasis on integrating spatial features inherent in CNNs and Transformers, ensuring that feature maps capture both long-range dependencies and local features. A hybrid CNN-Transformer architecture can effectively utilize the local features of CNNs while simultaneously modeling global features. TransUnet (Chen et al., 2021), as shown in Fig. 1 (a), is the first method to fuse U-shaped CNN architectures and Transformers in the field of medical image segmentation. It uses CNNs to extract high-resolution spatial details and contextual information, while the Transformer captures long-range dependencies in high-level features (Yuan et al., 2023). UNet, a method that alternates between CNNs and Transformers across encoder and decoder subnetworks at different resolutions to enhance segmentation performance (Gao et al., 2021;

He et al., 2023b), as shown in Fig. 1 (b). Yuan et al. (2023), proposed a dual encoder hybrid CNN transformer model, where both encoders extract features, which are subsequently fused and transmitted to the decoder for upsampling via skip connections, as illustrated in Fig. 1 (c). Additionally, they introduce a Feature Complementary Module (FCM) to perform spatial and channel-wise fusion of features with matching channel dimensions from both CNNs and Swin Transformers, aiming to enhance overall model performance. (Li et al., 2022) propose a TFCN model that integrates the transformer architecture into FCDenseNet (Jégou et al., 2017) at the encoder stage. Meanwhile, an RL-Transformer layer is introduced in the final stage of the encoder to enhance the receptive field, while a convolutional linear attention block is integrated into the skip connections to locate areas containing more effective information (Liu et al., 2023). HCT-Net, proposed by (He et al., 2023b), adds a Transformer Encoder Block (TEBlock) to certain encoder layers after a residual basic block to extract contextual information from the feature maps, and introduces Spatial-wise Cross Attention (SCA) to reduce the semantic discrepancy issue. TransFuse, proposed by (Zhang et al., 2021), features two independent encoders: a CNN and a transformer. While both encoders independently perform the segmentation task, their feature maps are fused through the BiFusion module and passed to the decoder. The decoder adopts the Progressive Upsampling (PUP) method to reconstruct the mask. This model effectively captures both global dependencies and low-level spatial details, leading to improved performance in segmentation tasks. Although these models have shown improved segmentation performance, they tend to focus excessively on spatial feature integration while overlooking channel attention between models.

2.4. Channel and Spatial Attention Mechanisms

Channel attention mechanisms enhance the importance of specific feature channels while suppressing others, enabling deep learning models to prioritize significant features. The SE Block, proposed by (Hu et al., 2018), aggregates the information during the squeeze process and captures channel-wise dependencies in the excitation process, which effectively boosts performance in classification tasks (Hu et al., 2018). The ECA module, proposed by (Wang et al., 2020), applies a 1D convolution with a specific kernel size K to effectively extract channel attention from the feature map. Compared to the SE Block, it uses fewer parameters, and the 1D convolution can adaptively adjust the weights of each channel (Wang et al., 2020). Both ECA-module and SE-Block only focus on the channel attention and ignore the spatial attention in the feature map. (Li et al., 2019) propose a selective kernel convolution that introduces a dynamic selection mechanism in convolutional neural networks (CNNs), enabling each neuron to adaptively modify its receptive field size based on various scales of input information. (Ates et al., 2023) propose a Dual Cross-Attention (DCA) block, which employs a multi-head attention mechanism to capture all channel correlations between multi-scale features and eliminate semantic gaps between multi-level features. However, overly dense attention mechanisms can lead to the model

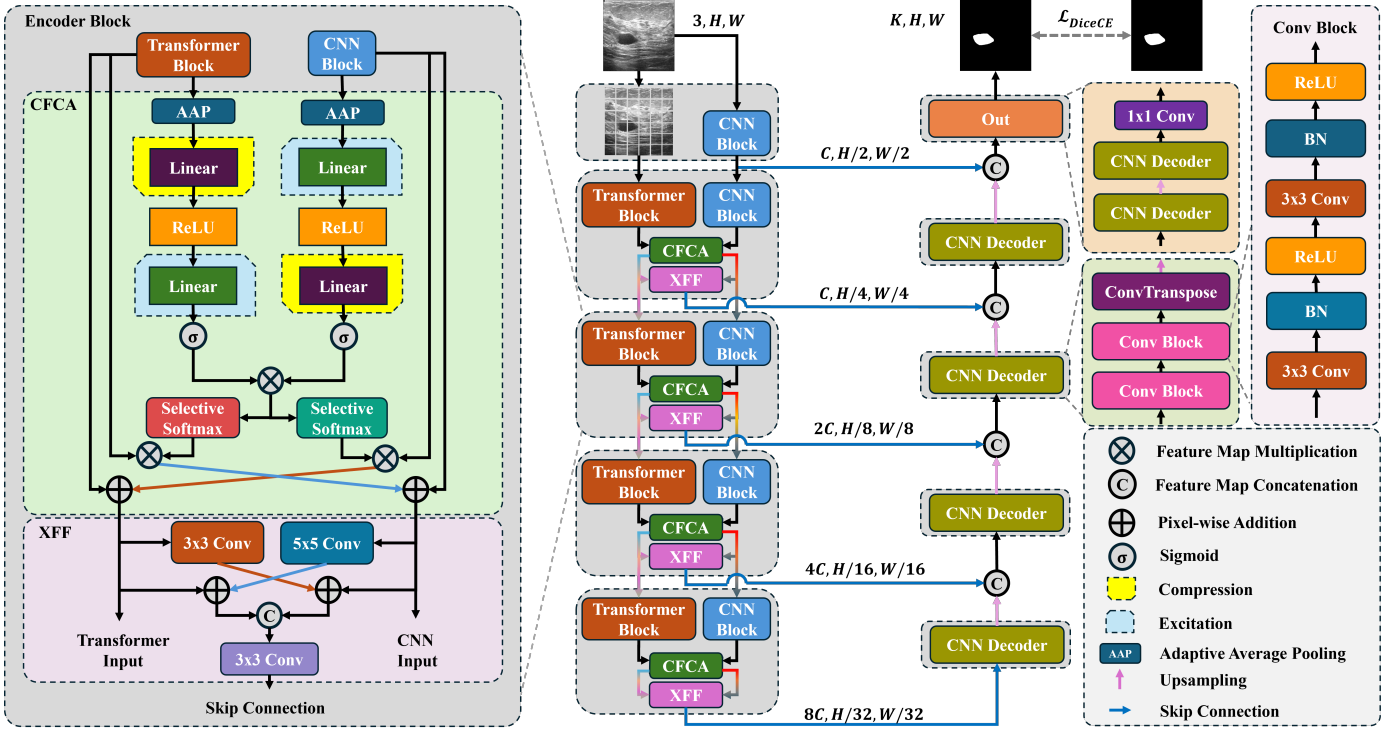


Fig. 2: The architecture of CFFormer and a detailed demonstration of the internal workings of the Cross-Feature Channel Attention (CFCA) module and the X-Spatial Feature Fusion (XFF) module. In the experiment, we set $C = 64$, representing 64 channels. K represents the number of classes in multi-class segmentation. For single-class segmentation, K should be 1.

processing excessive redundant information. Although attention mechanisms can improve the model’s ability to capture semantic information and expand the receptive field to some extent, they remain less effective than transformers in capturing global receptive fields.

3. Methodology

In our model, we employ two encoders: CNN and Transformer, aiming for the CNN to capture rich local features while enabling the Transformer to extract effective global information. Our model adopts a U-shaped architecture to mitigate information loss during the downsampling process. We propose a CFCA module to map the features from two encoders based on the channel correlations, enabling interaction on spatial feature information. Meanwhile, our XFF module achieves an effective fusion of CNN features and Transformer features.

3.1. Encoders

In our experiments, we utilize ResNet34 (He et al., 2016) as the framework for the CNN, while the Transformer is implemented as Swin Transformer V2 (Liu et al., 2022). Our goal is to utilize the CNN for extracting local features and the Transformer for modeling global features. The model consists of five layers, with the first layer utilizing a ResNet Block as the CNN block for feature extraction, while layers 2 to 5 concurrently employ both encoders to extract features as shown in Fig. 2. The outputs from the CNN and Transformer serve as inputs to the CFCA module for calculating cross-channel attention, and

the output of the CFCA module is then used as input for the subsequent layer of the decoder. Additionally, the embedding of our CFCA module supports other CNNs and Transformers as alternative backbone frameworks. Furthermore, the XFF module merges the outputs of the CFCA module, and its output constitutes a part of the decoder input for the corresponding layer.

3.1.1. Cross-Feature Channel Attention Module (CFCA)

Although CNNs excel at capturing rich local features and Transformers are adept at modeling comprehensive global features, their strengths are also complementary to each other’s weaknesses. To fully utilize the strengths of the encoders, we propose the CFCA module to supplement the missing information between the two encoders. This module extracts local features from the CNN and effectively integrates them into the Transformer’s features, while filtering the Transformer’s features and mapping them into the CNN’s feature space.

In detail, we refine two feature maps by constructing a correlation matrix based on their channel features. The CNN and Transformer modules first extract multi-channel feature maps $\mathbf{U} \in \mathbb{R}^{C_c \times W \times H}$ and $\mathbf{V} \in \mathbb{R}^{C_t \times W \times H}$ respectively, where C_c and C_t respectively denote the number of CNN and Transformer feature channels, and W and H respectively denote the width and height of feature maps. Directly constructing a channel correlation matrix between \mathbf{U} and \mathbf{V} introduces several challenges, including significant computational complexity and limited effectiveness in enhancing the internal channel attention of the feature maps. To improve computational efficiency and facilitate internal channel attention, we compress the multi-channel

feature maps into channel feature vectors whose elements can represent the individual channels' characteristics. To achieve the efficient compression, we adopt the adaptive average pooling (AAP) operator $\mathbf{F}_{\text{AAP}} : \mathbb{R}^{C \times W \times H} \rightarrow \mathbb{R}^{C \times 1}$ that maps the C -channel feature map into a C -dimensional vector, by calculating the average value of the feature map at each channel. Then, the multi-channel feature maps \mathbf{U} and \mathbf{V} can be compressed as

$$\mathbf{U}_{\text{AAP}} = \mathbf{F}_{\text{AAP}}(\mathbf{U}), \mathbf{V}_{\text{AAP}} = \mathbf{F}_{\text{AAP}}(\mathbf{V}), \quad (1)$$

where $\mathbf{U}_{\text{AAP}} \in \mathbb{R}^{C_c \times 1}$ and $\mathbf{V}_{\text{AAP}} \in \mathbb{R}^{C_t \times 1}$ are compressed channel feature vectors of \mathbf{U} and \mathbf{V} respectively.

In general cases, Transformer extracts more channels of feature maps than CNN, i.e., $C_t > C_c$. To make the compressed channel features \mathbf{U}_{AAP} and \mathbf{V}_{AAP} aware of each other's dimension and build the correlations between high- and low-channel features for the subsequent cross-channel attention, we respectively apply the excitation-then-compression and compression-then-excitation operations to the CNN channel feature vector \mathbf{U}_{AAP} and the Transformer channel feature vector \mathbf{V}_{AAP} to obtain their corresponding internal channel attention vectors $\mathbf{U}_{\text{Attn}} \in \mathbb{R}^{C_c \times 1}$ and $\mathbf{V}_{\text{Attn}} \in \mathbb{R}^{C_t \times 1}$. The excitation-then-compression operation first maps $\mathbf{U}_{\text{AAP}} \in \mathbb{R}^{C_c \times 1}$ to a higher C_t -dimensional space through a linear transformation with a weight matrix $\mathbf{W}_E \in \mathbb{R}^{C_t \times C_c}$ followed by the ReLU activation $\text{ReLU}(\cdot)$, then compresses it back to the original C_c -dimensional space by another linear transformation with a weight matrix $\mathbf{W}_C \in \mathbb{R}^{C_c \times C_t}$ followed by the Sigmoid activation $\sigma(\cdot)$:

$$\mathbf{U}_{\text{Attn}} = \sigma[\mathbf{W}_C \text{ReLU}(\mathbf{W}_E \mathbf{U}_{\text{AAP}})]. \quad (2)$$

Similarly, the compression-then-excitation operation first compresses $\mathbf{V}_{\text{AAP}} \in \mathbb{R}^{C_t \times 1}$ to a lower C_c -dimensional space through a linear transformation with the weight matrix $\mathbf{W}_C \in \mathbb{R}^{C_c \times C_t}$ followed by the the ReLU activation $\text{ReLU}(\cdot)$, then recovers it back the original C_t -dimensional space by another linear transformation with the weight matrix $\mathbf{W}_E \in \mathbb{R}^{C_t \times C_c}$ followed by the Sigmoid activation $\sigma(\cdot)$:

$$\mathbf{V}_{\text{Attn}} = \sigma[\mathbf{W}_E \text{ReLU}(\mathbf{W}_C \mathbf{V}_{\text{AAP}})]. \quad (3)$$

Then, we can construct the cross-feature channel correlation matrix $\mathbf{Q} \in \mathbb{R}^{C_c \times C_t}$ as:

$$\mathbf{Q} = \mathbf{U}_{\text{Attn}} \times \mathbf{V}_{\text{Attn}}^T. \quad (4)$$

With the correlation matrix \mathbf{Q} , we can identify the correlated channel features between the CNN and Transformer feature maps $\mathbf{U} \in \mathbb{R}^{C_c \times W \times H}$ and $\mathbf{V} \in \mathbb{R}^{C_t \times W \times H}$. By using \mathbf{Q} as a transformation matrix, we can project \mathbf{U} to a subspace that well correlates to \mathbf{V} , and project \mathbf{V} into a subspace that well correlates to \mathbf{U} :

$$\mathbf{U}_{\rightarrow \mathbf{V}} = \mathbf{U} \times_1 \text{Softmax}(\mathbf{Q}^T), \quad (5)$$

$$\mathbf{V}_{\rightarrow \mathbf{U}} = \mathbf{V} \times_1 \text{Softmax}(\mathbf{Q}), \quad (6)$$

where $\text{Softmax}(\cdot)$ is used to normalize channel correlations, \times_1 is the 1-mode tensor product (Kolda and Bader, 2009), $\mathbf{U}_{\rightarrow \mathbf{V}} \in \mathbb{R}^{C_t \times W \times H}$ and $\mathbf{V}_{\rightarrow \mathbf{U}} \in \mathbb{R}^{C_c \times W \times H}$ are respectively the projections

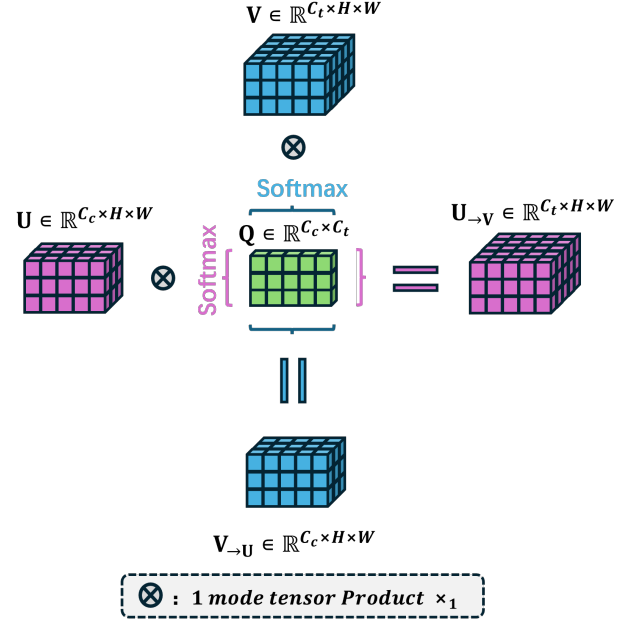


Fig. 3: An overview of the cross-feature channel attention projection procedure.

of \mathbf{U} and \mathbf{V} , i.e., channel feature compositions that correlate to \mathbf{V} and \mathbf{U} .

To enable the CNN feature maps to contain global information and address the Transformer feature maps' lack of local features, we directly add the projected features $\mathbf{U}_{\rightarrow \mathbf{V}}$ and $\mathbf{V}_{\rightarrow \mathbf{U}}$ to the original features \mathbf{V} and \mathbf{U} , thereby achieving feature fusion. The feature fusion is completed as follows:

$$\mathbf{U}_{\text{Fused}} = \mathbf{V}_{\rightarrow \mathbf{U}} + \mathbf{U}, \quad (7)$$

$$\mathbf{V}_{\text{Fused}} = \mathbf{U}_{\rightarrow \mathbf{V}} + \mathbf{V}, \quad (8)$$

where $\mathbf{U}_{\text{Fused}} \in \mathbb{R}^{C_c \times W \times H}$ represents the updated CNN feature maps fused by the Transformer features and $\mathbf{V}_{\text{Fused}} \in \mathbb{R}^{C_t \times W \times H}$ is the updated Transformer feature maps fused by the CNN features. They then act as the input for the XFF module as well as the next layer's CFCA module.

3.1.2. X-spatial Feature Fusion (XFF)

In addition to performing feature fusion on the channel level, we also fuse CNN and Transformer features at the spatial level to make them better complement each other. To fully integrate spatial features, we apply convolution to re-embed the features while maintaining a small number of parameters. This fusion process aims to eliminate significant spatial discrepancies. In detail, we apply a 5×5 convolution $\text{Conv}_{5 \times 5}(\cdot)$ to $\mathbf{U}_{\text{Fused}}$, transforming its feature dimensions from $\mathbb{R}^{C_c \times W \times H}$ to $\mathbb{R}^{C_t \times W \times H}$. This feature is then added to $\mathbf{V}_{\text{Fused}}$, where the 5×5 convolution provides a relatively large receptive field, effectively bridging the gap in receptive field size between the CNN and Transformer. Meanwhile, we employ a 3×3 convolution $\text{Conv}_{3 \times 3}(\cdot)$ on $\mathbf{V}_{\text{Fused}}$, mapping its dimensions from $\mathbb{R}^{C_t \times W \times H}$ to $\mathbb{R}^{C_c \times W \times H}$ using a smaller kernel size, then add it to $\mathbf{U}_{\text{Fused}}$. Ultimately, the fused results are concatenated and passed to an output convolution layer to produce input to the skip connection, where

a number of channels are used, effectively controlling the parameter count in the decoder. The procedure can be obtained by:

$$\mathbf{V}_{\text{Skip}} = \text{Conv}_{5 \times 5}(\mathbf{U}_{\text{Fused}}) + \mathbf{V}_{\text{Fused}}, \quad (9)$$

$$\mathbf{U}_{\text{Skip}} = \text{Conv}_{3 \times 3}(\mathbf{V}_{\text{Fused}}) + \mathbf{U}_{\text{Fused}}, \quad (10)$$

$$\mathbf{X}_{\text{Skip}} = \text{Conv}_{3 \times 3}(\text{Concat}(\mathbf{V}_{\text{Skip}}, \mathbf{U}_{\text{Skip}})), \quad (11)$$

where $\text{Concat}(\cdot, \cdot)$ denotes the operation of concatenating two feature maps, \mathbf{V}_{Skip} and \mathbf{U}_{Skip} , and \mathbf{X}_{Skip} represents the input to the skip connection. The dimension of the resulting feature map is controlled by the $\text{Conv}_{3 \times 3}(\cdot)$ operation, which projects the feature dimension into a specific number C_k , yielding a feature map of size $\mathbb{R}^{C_k \times W \times H}$.

3.2. Decoders

For the decoder, we adopt a simple architecture similar to U-Net to facilitate upsampling and mask generation as shown in Fig. 2. With the exception of the fifth layer of the CNN decoder, the inputs to all other decoder layers are formed by the concatenation of the output from the previous decoder layer and the skip connection output \mathbf{X}_{Skip} . Each up-sampling operation utilizes a dual convolution structure akin to that of the U-Net decoder, combined with a ConvTranspose operation to achieve up-sampling.

3.3. Loss Function

Feng et al. (2020) indicate that combining Dice loss with cross-entropy loss can address the common issue of class imbalance in medical image segmentation, thereby enhancing performance. To optimize our model, we employ a balanced joint loss of \mathcal{L}_{ce} and \mathcal{L}_{Dice} . The formulation of \mathcal{L}_{DiceCE} has been discussed in Dai et al. (2024), and is expressed as follows:

$$\mathcal{L}_{DiceCE} = \lambda \mathcal{L}_{ce} + (1 - \lambda) \mathcal{L}_{Dice}. \quad (12)$$

To balance the accuracy of pixel-level classification and the optimization of global regions, we set $\lambda = 0.5$. This weight ensures an equal contribution from both the \mathcal{L}_{ce} and \mathcal{L}_{Dice} during training, preventing the model from overly focusing on pixel-level classification. When $\lambda > 0.5$, the model tends to prioritize the consistency of global segmentation regions, potentially overlooking fine-grained pixel-level classification. Conversely, when $\lambda < 0.5$, the model may perform better in pixel-level classification but fail to sufficiently optimize the consistency of global segmentation regions. To ensure fairness in the experiments, we will use \mathcal{L}_{DiceCE} for all models.

4. Experiments and Results

4.1. Implementation Details

To mitigate overfitting and improve the model’s generalization capability, we apply several data augmentation techniques, including random cropping with a scale of 0.5, random horizontal flip with a probability of 0.5, random vertical flip with a probability of 0.5, and random rotation of ± 15 degrees with a probability of 0.6. Normalization is performed

with a mean of [0.485, 0.456, 0.406] and a standard deviation of [0.229, 0.224, 0.225]. These augmentation strategies are applied across all datasets except the Synapse dataset. Our experiments are conducted using the PyTorch framework, and all models are trained and tested on NVIDIA A5000 GPUs. We set the random seed to 42 for all models, dataloader’s worker initialization and fetch, as well as for data splits. The number of epochs is set to 130, including 10 warm-up epochs and 120 epochs for training. We utilize the AdamW optimizer with a weight decay of 3×10^{-5} and betas of (0.9, 0.999). The initial learning rate is set to 0.0003, and we employ a “Poly” learning rate policy with a power of 0.9. We will release our code on GitHub.

4.2. Datasets

In our experiments, all medical images in the dataset are resized to 224×224 , and the batch size for datasets is set to 16. We utilize the following eight datasets to train and evaluate the models’ performance.

- The **BUSI** data includes breast ultrasound images collected from women aged between 25 and 75 years, containing images from 600 patients, with a total of 780 images and an average image size of 500×500 pixels. Among these, there are 437 benign images, 210 malignant images, and 133 normal images (Al-Dhabyani et al., 2020). We remove the normal cases to satisfy the medical image segmentation task. We extract 80% of the images from both benign and malignant cases for the training set, while the remaining 20% are randomly split into the validation and test sets in equal proportions.
- The UDIAT Diagnostic Centre of the Parc Taulí Corporation in Sabadell, Spain, has contributed **Dataset B**, with images collected using a Siemens ACUSON Sequoia C512 system with a 17L5 HD linear array transducer. It contains 163 breast ultrasound images from various women, each featuring one or more lesions, with an average image size of 760×570 pixels (Yap et al., 2017). We randomly sample 80% of the dataset for the training set, 10% for the validation set, and the remaining 10% is used as the test set.
- Melanoma is one of the most lethal forms of skin cancer. In 2016, melanoma led to over 10,000 deaths from this cancer. The **ISIC-2016** challenge consists of three tasks: the Lesion Segmentation Task, the Dermoscopic Feature Classification Task, and the Disease Classification Task (Gutman et al., 2016). In our experiments, we use the Lesion Segmentation Task dataset, which contains 900 training dermoscopic images and 379 testing dermoscopic images.
- The **PH2** database comprises 200 dermoscopic images provided by (Mendonça et al., 2013), including 80 normal nevi, 80 atypical nevi, and 40 melanoma cases. Both normal nevi and atypical nevi are categorized as non-melanoma. To mitigate data imbalance, we sample 80% of the 160 non-melanoma images and 80% of the 40

Table 1: A Summary of the Datasets

Dataset	# Images	Resize	Train	Valid	Test	Modality
BUSI (Al-Dhabyani et al., 2020)	647	(224,224)	517	65	65	Ultrasound Images
Dataset B (Yap et al., 2017)	160	(224,224)	128	17	16	Ultrasound Images
ISIC2016 (Gutman et al., 2016)	1279	(224,224)	900	N/A	379	Dermoscopy Images
PH2 (Mendonça et al., 2013)	200	(224,224)	160	20	20	Dermoscopy Images
Synapse (Landman et al., 2015)	30	(224,224)	18	6	6	CT
Kvasir Seg (Jha et al., 2020)	1000	(224,224)	800	100	100	Colon polyp images
CVC-Clinic (Zhou et al., 2019)	612	(224,224)	489	61	62	Colon polyp images
Brain-MRI (Buda et al., 2019)	1373	(224,224)	1098	137	138	MRI Images

melanoma images to form the training set, with the remaining 20% designated for the validation and test sets in equal proportions.

- The **Synapse** dataset comprises 30 abdominal CT scans sourced from the MICCAI 2015 Multi-Atlas Abdomen Labeling Challenge (Landman et al., 2015). For segmentation purposes, we follow the same dataset setup as TransUnet(Chen et al., 2021), focusing on 8 organs: the aorta, gallbladder, spleen, left kidney, right kidney, liver, pancreas, and stomach. Each CT volume contains 85-198 slices. The dataset is divided into 18 volumes for training. Unlike TransUnet(Chen et al., 2021), which uses the remaining 12 volumes solely for testing, we split these 12 volumes into 6 for validation and 6 for testing. This approach provides a more robust evaluation of the model’s generalization capability.
- Colorectal cancer is the second most prevalent cancer among women and the third among men. Polyps are early indicators of this cancer, so automatically detecting polyps at an initial stage is crucial for improving both prevention and survival outcomes. The **Kvasir-SEG** dataset provides 1000 annotated images of colon polyps, with resolutions varying from 332×487 to 1920×1072 pixels (Jha et al., 2020). We randomly sample 80% of the dataset for the training set and equally divide the remaining 20% into the validation and test sets.
- The **CVC-ClinicDB** dataset comprises 612 frames extracted from 25 colonoscopy videos, capturing various instances of polyps (Zhou et al., 2019). For 2D segmentation, we randomly chose 80% of the dataset for training, while the remaining 10% is assigned to testing and 10% to validation.
- The LGG Segmentation dataset (TCGA-LGG) is sourced from The Cancer Imaging Archive (TCIA) and includes a collection of lower-grade glioma cases with minimal Fluid-Attenuated Inversion Recovery (FLAIR) effects. This **Brain-MRI** dataset provides MRI scans for brain segmentation, capturing genomic tumor clusters from 110 patients (Buda et al., 2019). It consists of 3929 images. After removing all positive cases, we randomly select 80% of the remaining 1,373 negative cases for the training set, with the final 20% equally allocated to the validation and test sets.

The significant disparities in data volume and the considerable variations in modalities among these datasets enable a comprehensive evaluation of the model’s stability in performance across different data sizes and modalities. A summary of the datasets is provided in Table. 1.

4.3. Evaluation Metrics and Comparison Methods

In our experiments, we employ multiple evaluation metrics to rigorously assess model performance across diverse modalities, including Dice, Jaccard, and Hausdorff Distance at the 95th percentile (HD95). The specific description of key evaluation metrics is discussed as follows:

- **Dice**: Dice similarity coefficient measures the overlap between predicted and ground truth segmentations, and it is particularly effective in handling class imbalance. A Higher Dice score indicates better similarity between predicted segmentation results and ground truth.
- **Jaccard**: Jaccard evaluates the similarity between predicted and ground truth segmentation, penalizing both false positives and false negatives more strictly than Dice. A higher Jaccard score indicates better segmentation performance.
- **HD95**: Hausdorff Distance at the 95th percentile (HD95) quantifies the spatial distance between the boundaries of predicted and ground truth segmentations, focusing on the largest deviations while ignoring extreme outliers. A lower HD95 value indicates that the boundaries of the predicted segmentation are closer to the true boundaries in ground truth segmentation.

To evaluate the efficiency of the model in real-world applications and its computational resource requirements, we employ GPU memory usage and Frames Per Second (FPS) as the primary evaluation metrics. We do not consider the Number of Parameters as a standard metric since the parameter count does not directly reflect the actual storage demands or runtime efficiency of a model. For instance, sparsity in the weight matrix may result in a higher parameter count, yet the memory footprint remains negligible. Moreover, while FLOPs is an essential measure of computational complexity, it does not necessarily correlate with the actual inference speed. The practical performance often depends on the degree of model optimization and the underlying hardware support. Therefore, using GPU memory usage and FPS as evaluation metrics provides a more intuitive and accurate characterization of the model’s real-world

Table 2: Quantitative comparison of the proposed method’s performance with SOTA methods on the BUSI and Dataset B. **Red** indicates the best results, **Blue** is the second-best, and * denotes models utilizing pre-trained parameters. → represents the domain-shift experiment, where the arrow indicates the test set.

Types	Model	BUSI			Dataset B			BUSI→Dataset B		
		Dice↑	Jaccard↑	HD95↓	Dice↑	Jaccard↑	HD95↓	Dice↑	Jaccard↑	HD95↓
CNNs	U-Net (Ronneberger et al., 2015)	78.51	68.85	18.48	78.50	71.33	15.60	78.49	69.48	13.19
	Attention U-Net (Oktay et al., 2018)	81.43	72.69	10.21	78.14	70.89	16.10	74.18	64.58	27.18
	ResUnet (Diakogiannis et al., 2020)	67.18	57.30	31.93	70.56	60.61	18.69	67.12	56.85	34.60
	FATnet (Wu et al., 2022)	82.69	73.41	9.78	82.82	74.31	11.54	74.37	64.72	20.63
	DCSAUnet (Xu et al., 2023)	81.88	72.15	9.01	58.56	46.42	35.09	69.27	60.96	23.91
	M ² Snet* (Zhao et al., 2023)	84.26	75.00	9.01	83.45	76.03	10.11	85.76	77.44	7.34
	CMUNeXt-Large (Tang et al., 2024)	82.79	73.38	8.75	68.95	57.83	20.40	69.10	59.89	31.79
	I2U-net-Large (Dai et al., 2024)	82.72	73.36	9.46	81.07	72.72	10.22	74.09	65.35	22.82
Hybrid Models	MISSFormer (Huang et al., 2021)	76.69	66.89	14.78	79.05	70.41	13.45	77.12	67.13	19.91
	Trans-Unet* (Chen et al., 2021)	82.60	74.22	10.68	80.50	72.27	13.38	88.01	80.95	5.77
	HiFormer-Base* (Heidari et al., 2023)	82.99	74.59	9.02	85.57	76.23	8.53	84.12	74.65	6.01
	H2Former* (He et al., 2023a)	84.92	76.06	8.04	81.21	71.79	13.34	79.63	70.40	13.16
	BEFUnet* (Manzari et al., 2024)	81.88	72.01	9.30	78.06	68.94	18.33	78.71	67.91	15.01
	CFFormer* (Ours)	86.23	77.87	7.48	87.94	79.24	3.47	89.52	81.81	4.01

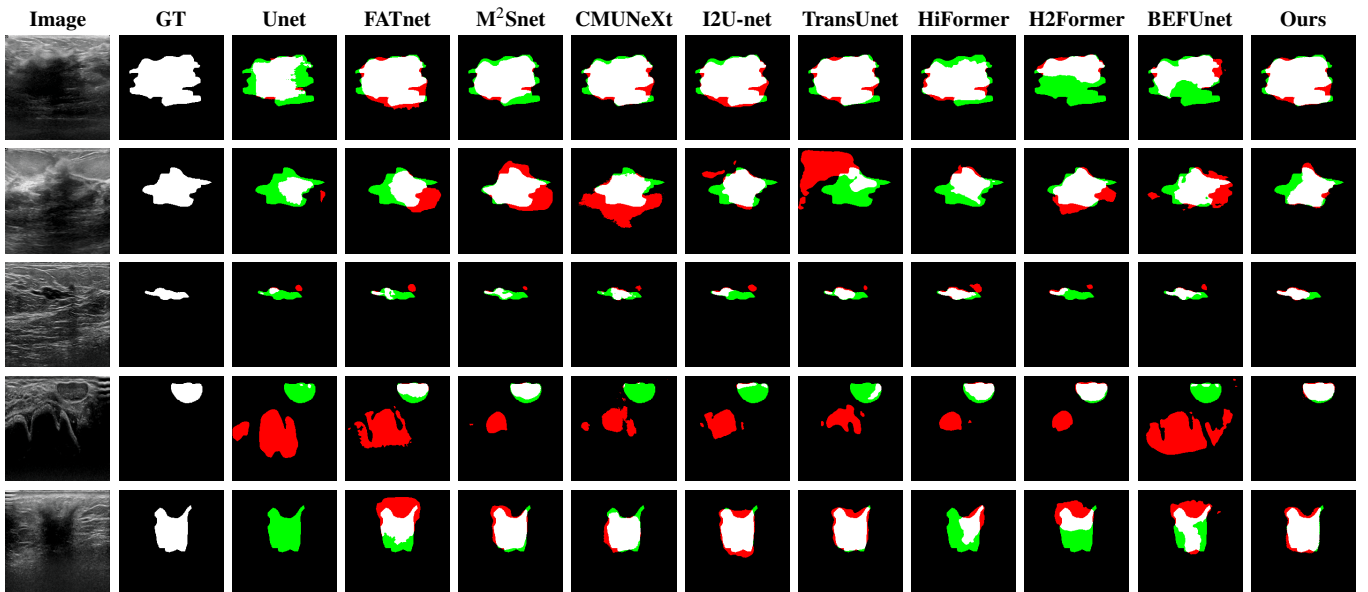


Fig. 4: Visualisation results: The first two rows show the model’s performance on BUSI, the third and fourth rows on Dataset B, and the last row performs the visualisation results of Domain-Shift results. Red represents over-segmentation, green under-segmentation, and white correct segmentation.

performance, making this approach more compelling and relevant for practical applications.

To ensure comprehensive benchmarking, we compare our model against a variety of state-of-the-art (SOTA) methods, incorporating CNN-based and hybrid CNN-Transformer architectures. For all transformer-based and hybrid CNN-Transformer models, we utilize their pretrained weights to maintain experimental rigor and ensure fair comparisons. The CNN-based models include U-Net (Ronneberger et al., 2015), Attention U-Net (Oktay et al., 2018), ResUnet (Diakogiannis et al., 2020), FATnet (Wu et al., 2022), DCSAUnet (Xu et al., 2023), M²Snet (Zhao et al., 2023), CMUNeXt-Large (Tang et al., 2024), and I2U-Net-Large (Dai et al., 2024), while the hybrid CNN-Transformer models encompass MISSFormer (Huang et al., 2021), TransUnet (Chen et al., 2021), HiFormer (Base Version) (Heidari et al., 2023), H2Former (He et al., 2023a) and BEFUnet (Manzari et al., 2024).

4.4. Task 1: Breast Ultrasound Image Segmentation

Breast ultrasound images typically exhibit characteristics such as intensity distributions, blurred boundaries, and irregular tumor morphology, which can indirectly impact the model’s performance (Zhang et al., 2024). Consequently, this presents a significant challenge to the model’s ability to capture global features effectively.

The quantitative and visualisation results for breast ultrasound image segmentation are presented in Tables 2 and Fig. 4. Our model achieves the best performance in Dice, Jaccard, and HD95 metrics on both the BUSI dataset and Dataset B. As shown in Table 2, in the BUSI dataset, our model surpasses the SOTA model H2Former (He et al., 2023a) by 1.31% in Dice, 1.81% in Jaccard, and achieves a lower HD95 of 7.48. Meanwhile, in Dataset B, our model also surpasses the SOTA model HiFormer-Base (Heidari et al., 2023) by 2.37% in Dice, 3.01% in Jaccard, and an HD95 of 3.47.

Table 3: Quantitative results of the proposed method’s performance with SOTA methods on the ISIC-2016 and PH2 Dataset. **Red** indicates the best results, **Blue** is the second-best, and * denotes models utilizing pre-trained parameters. → represents the domain-shift experiment, where the arrow indicates the test set.

Types	Model	ISIC-2016			PH2			ISIC-2016→PH2		
		Dice↑	Jaccard↑	HD95↓	Dice↑	Jaccard↑	HD95↓	Dice↑	Jaccard↑	HD95↓
CNNs	U-Net (Ronneberger et al., 2015)	90.57	84.14	4.62	92.26	85.89	3.21	88.69	81.09	6.98
	Attention U-Net (Oktay et al., 2018)	90.75	84.44	4.22	92.70	86.68	2.73	88.00	79.97	7.85
	ResUnet (Diakogiannis et al., 2020)	88.64	81.51	7.38	91.50	84.83	6.56	87.40	78.70	5.87
	FATnet (Wu et al., 2022)	91.67	85.65	3.21	93.11	87.35	2.21	90.40	83.23	4.46
	DCSAUnet (Xu et al., 2023)	90.61	84.23	4.13	92.10	85.71	2.84	89.50	82.39	6.72
	M ² Snet* (Zhao et al., 2023)	91.84	85.85	3.21	94.79	90.27	1.46	91.10	84.49	3.19
	CMUNeXt-Large (Tang et al., 2024)	90.58	84.15	4.29	91.62	85.02	2.83	86.08	77.01	7.76
	I2U-net-Large (Dai et al., 2024)	90.94	84.74	4.19	94.17	89.13	1.67	89.38	82.13	5.82
Hybrid Models	MISSFormer (Huang et al., 2021)	90.69	84.44	4.19	92.52	86.47	2.35	88.07	79.98	5.51
	Trans-Unet* (Chen et al., 2021)	91.87	85.77	3.70	94.76	90.30	1.70	90.58	83.75	3.69
	HiFormer-Base* (Heidari et al., 2023)	91.83	85.77	3.30	94.49	89.74	1.79	91.69	85.28	2.74
	H2Former* (He et al., 2023a)	91.83	85.90	3.32	93.93	88.81	2.06	89.31	81.83	5.73
	BEFUnet* (Manzari et al., 2024)	91.62	85.43	3.64	92.24	86.27	2.54	89.48	81.89	3.92
	CFFormer* (Ours)	92.20	86.55	3.06	95.14	90.85	0.82	90.62	83.94	3.93

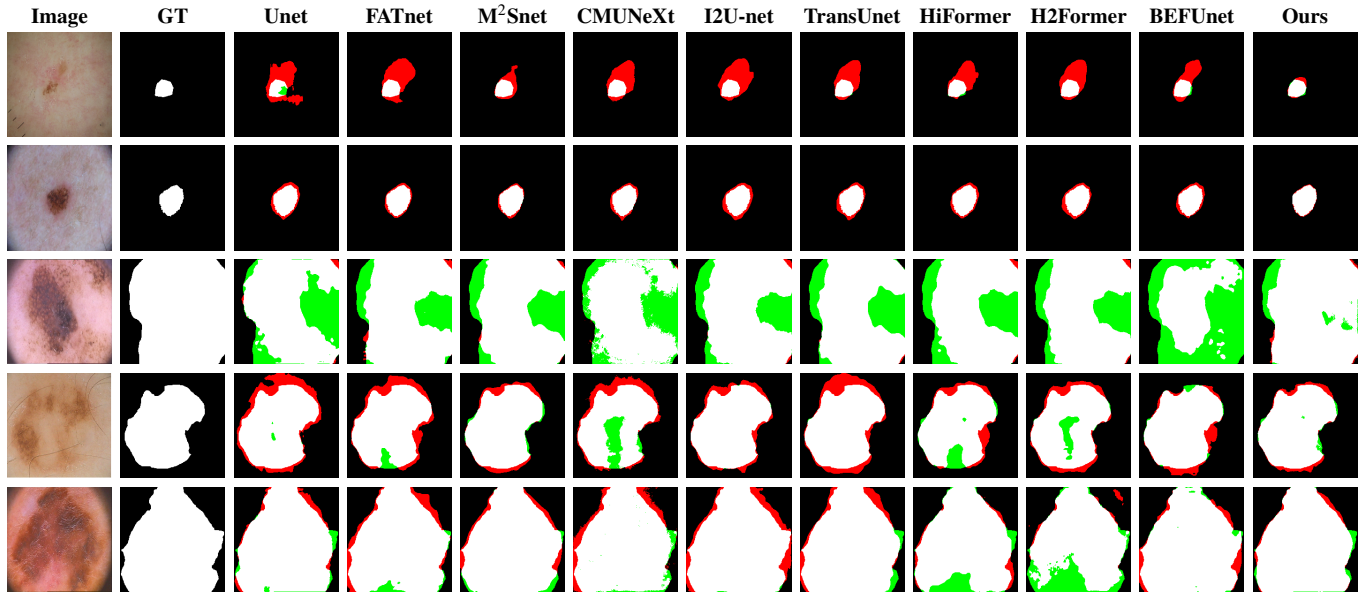


Fig. 5: Visualisation results: The first two rows show the model’s performance on ISIC-2016 dataset, the third and fourth rows on PH2, and the last row performs the visualisation results of Domain-Shift results. Red represents over-segmentation, green under-segmentation, and white correct segmentation.

To assess the generalization ability of the model, we conduct a domain shift experiment where the model is trained on the relatively large BUSI dataset and tested on Dataset B. The results show that our model’s domain shift performance outperforms the performance of the model trained directly on Dataset B across all metrics. As shown in Table 2, we observe significant improvements in the metrics only for M²Snet (Zhao et al., 2023), TransUnet (Chen et al., 2021), and our model, while the performance of other models either remained unchanged or decreased. This indicates that there is still a noticeable data distribution discrepancy between the two datasets, and the other models suffer from issues related to either excessive or insufficient model complexity. These issues significantly limit the application of these models in real-world medical image segmentation tasks. In the domain shift experiment, our model outperforms the SOTA model TransUnet, achieving Dice, Jaccard, and HD95 scores of 89.52, 81.81, and 4.01, respectively.

4.5. Task 2: Dermoscopy Image Segmentation

Compared to ultrasound images, dermoscopy images offer higher resolution and less noise, resulting in superior image quality and more distinct color characteristics. In the experiments, we employ a relatively large dataset, ISIC-2016 (Gutman et al., 2016), alongside a smaller dataset, PH2 (Mendonça et al., 2013), to evaluate our model’s segmentation performance. In this experiment, we continue to evaluate the generalization ability of the model through a domain-shift scenario. Although both datasets focus on melanoma segmentation, the PH2 dataset includes a greater variety of non-melanoma samples, such as 80 common nevi and atypical nevi. This setup challenges the model’s ability to generalize and its performance in segmenting outlier data. The results are displayed in Table 3 and Fig. 5, respectively.

Table 4: Quantitative results of the proposed method’s performance with SOTA methods on the Kvasir SEG and CVC-Clinic Dataset. **Red** indicates the best results, **Blue** is the second-best, and * denotes models utilizing pre-trained parameters. → represents the domain-shift experiment, where the arrow indicates the test set.

Types	Model	Kvasir SEG			CVC-ClinicDB			Kvasir SEG→CVC-ClinicDB		
		Dice↑	Jaccard↑	HD95↓	Dice↑	Jaccard↑	HD95↓	Dice↑	Jaccard↑	HD95↓
CNNs	U-Net (Ronneberger et al., 2015)	85.20	76.97	18.14	88.06	81.20	5.06	65.00	54.18	33.43
	Attention U-Net (Oktay et al., 2018)	85.06	77.08	16.62	87.26	81.27	5.12	68.01	57.93	39.28
	ResUnet (Diakogiannis et al., 2020)	80.17	69.74	24.56	84.81	77.40	11.10	65.85	54.18	33.43
	FATnet (Wu et al., 2022)	84.84	76.93	16.93	89.04	83.05	6.45	68.01	57.93	39.28
	DCSAUnet (Xu et al., 2023)	82.01	73.23	14.85	85.51	78.80	5.28	66.75	56.01	27.32
	M ² Snet* (Zhao et al., 2023)	89.18	82.70	11.73	93.47	88.18	2.65	78.84	71.53	11.21
	CMUNeXt-Large (Tang et al., 2024)	79.10	69.55	20.44	85.90	78.22	8.76	63.73	53.10	29.55
	I2U-net-Large (Dai et al., 2024)	83.98	75.96	14.67	89.66	82.97	3.18	69.31	58.81	31.72
Hybrid Models	MISSFormer (Huang et al., 2021)	82.36	73.52	17.90	90.50	83.53	4.50	75.26	65.22	28.28
	Trans-Unet* (Chen et al., 2021)	90.00	83.26	7.92	92.92	87.20	2.20	78.49	70.29	16.47
	HiFormer-Base* (Heidari et al., 2023)	89.11	82.68	11.84	92.11	86.99	3.03	78.90	71.10	8.35
	H2Former* (He et al., 2023a)	88.61	82.08	10.04	92.17	87.14	3.32	78.02	69.54	10.47
	BEFUnet* (Manzari et al., 2024)	83.96	95.46	12.45	88.32	80.26	5.62	74.63	64.46	20.03
	CFFormer* (Ours)	91.93	86.25	5.73	93.86	88.71	1.77	80.29	71.80	12.74

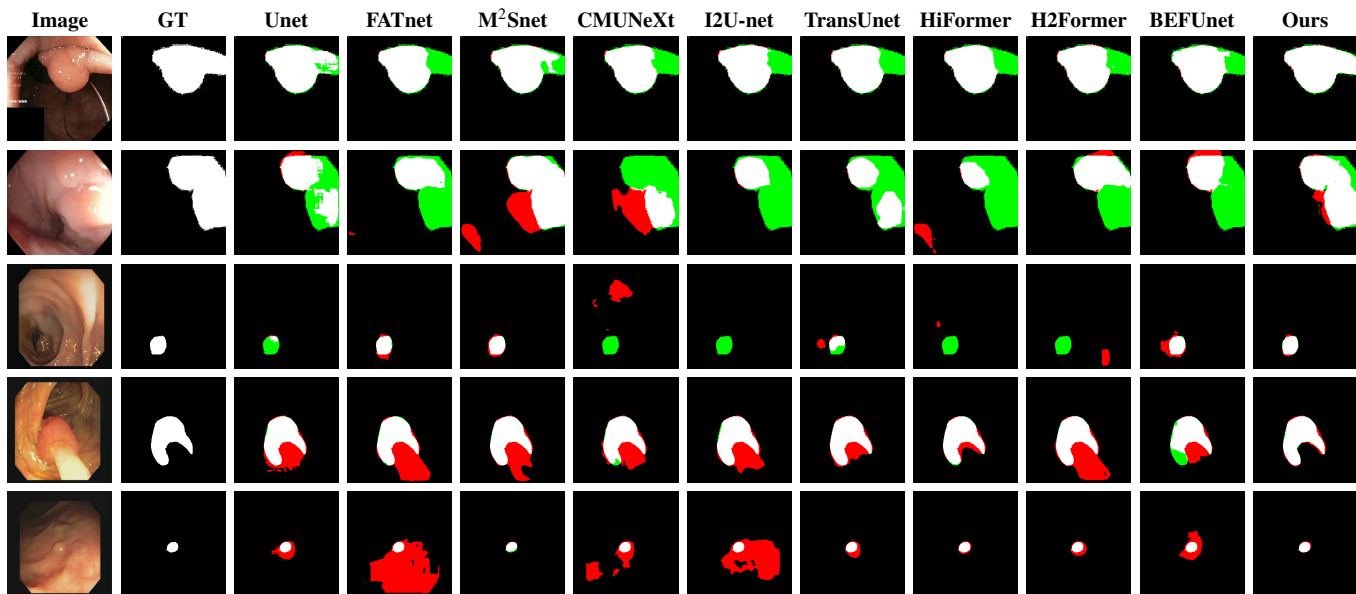


Fig. 6: Visualisation results: The first two rows show the model’s performance on Kvasir SEG, the third and fourth rows on CVC-ClinicDB, and the last row performs the visualisation results of Domain-Shift results. Red represents over-segmentation, green under-segmentation, and white correct segmentation.

In the ISIC-2016 dataset (Gutman et al., 2016), most models achieve strong segmentation performance, indicating relatively low data complexity. Upon analysis, we observe that CNN-based models perform comparably to hybrid models, suggesting that the dataset’s well-defined boundaries and pronounced color contrasts are particularly advantageous for CNN architectures. Furthermore, our model achieves state-of-the-art performance, with Dice, Jaccard, and HD95 scores of 92.20, 86.55, and 3.06, respectively. Meanwhile, on the PH2 dataset (Mendonça et al., 2013), which includes a greater diversity of lesion types, our model outperforms existing methods with Dice, Jaccard, and HD95 scores of 95.14, 90.85, and 0.82, respectively.

In the domain-shift experiments, our model ranks third on average across all metrics, demonstrating competitive generalization capabilities and robust segmentation performance when dealing with outlier data. This highlights its effectiveness in

handling cross-domain challenges in medical image segmentation.

4.6. Task 3: Colon Polyp Image Segmentation

Colon polyp medical images display significant variability in polyp shapes, sizes, colors, locations, and texture, which introduces substantial challenges for models in accurately capturing semantic features and delineating boundaries. In this study, we assess our model’s segmentation performance on two datasets, Kvasir-SEG (Jha et al., 2020) and CVC-ClinicDB (Zhou et al., 2019), where Kvasir-SEG provides approximately twice the sample size of CVC-ClinicDB. The comparative and domain-shift results are summarized in Table 4 and Fig. 6.

In Table 4, our model demonstrates excellent segmentation performance on polyp images. On the Kvasir SEG dataset (Jha et al., 2020), we surpass the SOTA models by 1.93% in Dice and 2.99% in Jaccard, with the lowest HD95 of 5.73. On the

Table 5: Comparison of the proposed method’s performance with state-of-the-art approaches on Synapse dataset. **Red** indicates the best results, **Blue** is the second-best, and * denotes models utilizing pre-trained parameters.

Types	Models	Spleen		Kidney(R)		Kidney(L)		Gallbladder		Pancreas		Liver		Stomach		Aorta		Average	
		Dice \uparrow	HD95 \downarrow	Dice \uparrow	HD95 \downarrow	Dice \uparrow	HD95 \downarrow	Dice \uparrow	HD95 \downarrow	Dice \uparrow	HD95 \downarrow	Dice \uparrow	HD95 \downarrow	Dice \uparrow	HD95 \downarrow	Dice \uparrow	HD95 \downarrow	Dice \uparrow	HD95 \downarrow
CNNs	U-Net (Ronneberger et al., 2015)	84.74	32.76	77.05	4.38	84.82	32.71	53.85	10.05	55.10	7.51	92.96	10.21	76.15	12.93	91.28	5.97	76.99	14.35
	Attention U-Net (Oktay et al., 2018)	88.50	6.30	88.61	32.74	86.90	13.11	28.45	3.75	58.75	8.70	94.66	11.51	76.07	15.22	89.57	2.86	76.19	11.77
	ResUnet (Diakogiannis et al., 2020)	90.65	35.67	84.89	15.28	87.38	44.01	53.44	13.98	52.26	11.57	93.74	36.92	78.21	17.98	87.95	4.69	78.56	22.51
	FATnet (Wu et al., 2022)	92.01	18.05	85.45	13.32	88.38	22.01	48.88	5.60	55.83	9.24	94.79	5.95	79.40	14.15	88.55	3.90	79.16	11.53
	DCSAUnet (Xu et al., 2023)	88.49	14.85	89.72	2.71	87.49	15.91	62.14	8.49	48.47	12.69	94.47	13.87	79.13	12.60	87.87	1.84	79.72	10.37
	M ² Snet* (Zhao et al., 2023)	90.92	5.84	83.65	2.56	91.01	23.37	55.42	12.14	60.42	6.64	94.95	3.80	81.46	9.74	84.84	2.07	80.33	8.27
	CMUNeXt-Large (Tang et al., 2024)	87.18	33.90	75.36	22.70	78.03	21.82	52.62	8.75	60.92	8.91	92.83	7.07	79.63	13.46	90.35	2.00	77.11	14.83
	I2U-net-Large (Dai et al., 2024)	88.38	22.58	86.98	3.203	88.59	32.99	54.60	8.00	52.24	9.00	94.56	8.70	75.09	13.03	84.62	3.81	78.13	12.66
Hybrid Models	MISSFormer (Huang et al., 2021)	92.40	26.59	87.20	14.57	88.58	27.06	57.96	20.74	50.86	9.56	94.76	9.48	73.51	13.60	87.35	1.57	79.08	15.40
	Trans-Unet* (Chen et al., 2021)	89.36	18.50	91.51	6.17	90.84	16.49	57.21	12.93	62.85	6.04	94.95	7.52	78.80	10.15	86.92	6.68	81.56	10.56
	HiFormer-Base* (Heidari et al., 2023)	92.39	3.72	86.75	19.48	90.40	12.32	54.27	9.19	65.02	6.01	94.85	8.72	78.63	9.97	88.47	1.89	81.35	8.91
	H2Former* (He et al., 2023a)	94.52	10.58	90.58	7.77	94.08	11.58	52.44	13.17	56.66	7.44	94.84	13.04	79.28	11.32	90.46	4.30	81.61	9.90
	BEFUnet* (Manzari et al., 2024)	82.37	65.92	79.36	14.71	78.09	46.69	49.59	9.37	49.93	12.31	90.61	21.90	70.29	18.83	84.82	8.50	73.13	24.78
	CFFormer* (Ours)	93.24	4.92	91.63	15.62	92.28	10.27	59.34	6.17	63.17	9.05	95.41	5.13	84.96	16.69	89.05	3.41	83.64	8.90

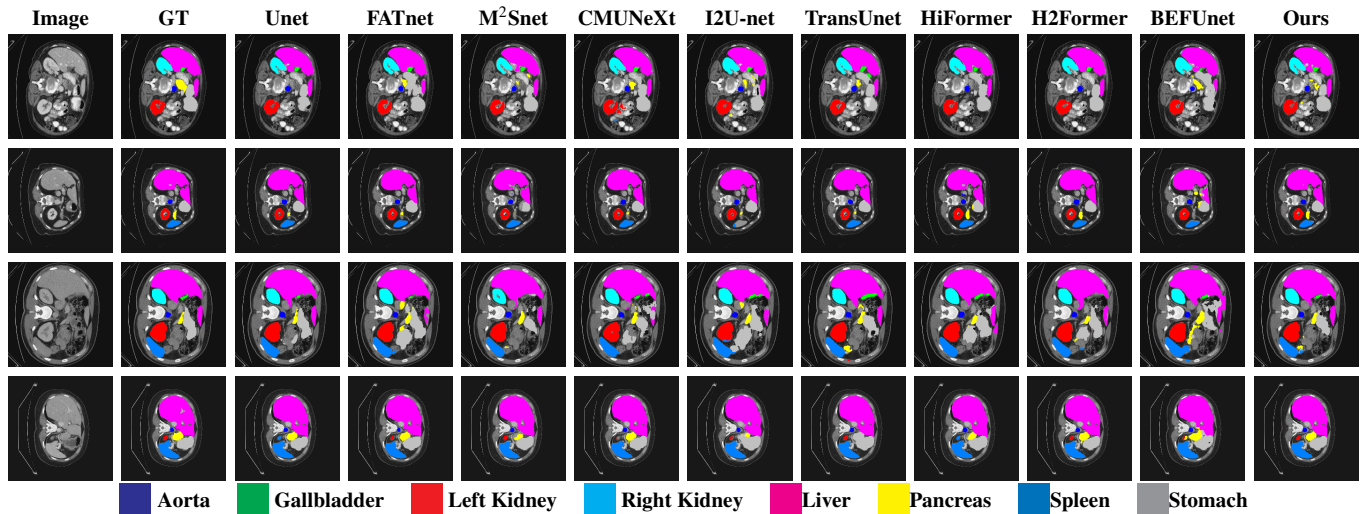


Fig. 7: Visualisation of Synapse Multi-Organ Medical Image Segmentation.

CVC-ClinicDB dataset, we outperform M²Snet across all metrics, achieving Dice, Jaccard, and HD95 values of 93.86, 88.71, and 1.77, respectively. In the domain-shift experiment, we first train the model on the Kvasir SEG dataset (Jha et al., 2020) and then test it on the CVC-ClinicDB dataset (Zhou et al., 2019). The results show that the performance of all models is inferior in the domain-shift experiment compared to direct training on CVC-ClinicDB (Zhou et al., 2019), which is due to the dataset’s inherent differences. Our model maintains SOTA performance even after domain shift, fully demonstrating its generalization capability.

4.7. Task 4: CT Image Segmentation

We selected the Synapse dataset (Landman et al., 2015) to evaluate the model’s performance on multi-class segmentation tasks. The significant morphological differences between organs and tissues, along with the fact that the data is derived from 3D scans where not every CT image includes all organs, present substantial challenges for the model in learning spatial relationships and contextual information. Table 5 demonstrates our model’s performance on the multi-organ segmentation task using the Synapse dataset, while Fig. 7 presents some of the visualisation results.

The results show that our model outperforms H2Former (He et al., 2023a) by an average Dice score of 2.03% across 8 or-

gans, with an average HD of 8.90. In the segmentation challenge for the 8 organs, our model surpasses the SOTA on Right Kidney, Liver, and Stomach, achieving Dice scores of 91.63, 95.41, and 84.96, respectively. Additionally, we achieve the second-best performance on Spleen, Left Kidney, Gallbladder, and Pancreas. Our model’s performance on the Aorta is also highly competitive. Therefore, through the multi-class segmentation challenge, our model demonstrates the ability to handle complex variations and exhibits strong generalization. By integrating feature maps from both CNN and Transformer, the model’s ability to learn contextual information is significantly enhanced.

4.8. Task 5: Brain MRI Image Segmentation

Irregular shapes, heterogeneity, and low contrast remain significant challenges in brain tumor MRI image segmentation. In this study, we utilize a brain MRI segmentation dataset to evaluate the model’s capacity to capture contextual and semantic information. The experimental results are presented in Table 6 and some visualisation results are presented in Fig. 8.

Our model outperforms state-of-the-art (SOTA) performance across multiple metrics, including Dice, Jaccard, recall, pixel accuracy and HD95. Specifically, our model surpasses the HiFormer-Base (Heidari et al., 2023) by 0.59% in Dice, achieving a score of 88.18, and outperforms H2Former (He et al.,

Table 6: Comparison of the proposed method’s performance with state-of-the-art approaches on Brain Tumor MRI dataset. **Red** indicates the best results, **Blue** the second-best, and * denotes models utilizing pre-trained parameters.

Types	Model	Dice \uparrow	Jaccard \uparrow	Precision \uparrow	Recall \uparrow	Pixel Accuracy (PA) \uparrow	HD95 \downarrow
CNNs	U-Net (Ronneberger et al., 2015)	86.51	77.80	87.43	88.40	99.49	3.11
	Attention U-Net (Oktay et al., 2018)	86.77	78.08	86.88	89.34	99.49	2.40
	ResUNet (Diakogiannis et al., 2020)	85.70	76.75	86.74	87.93	99.45	3.58
	FATnet (Wu et al., 2022)	86.48	78.04	86.93	88.37	99.51	2.35
	DCSAUnet (Xu et al., 2023)	87.55	79.04	87.56	89.57	99.52	2.10
	M ² Snet* (Zhao et al., 2023)	87.55	79.19	86.91	90.24	99.52	2.26
	CMUNeXt-Large (Tang et al., 2024)	86.99	78.25	87.30	88.85	99.50	2.15
	I2U-net-Large (Dai et al., 2024)	86.27	77.34	86.20	88.68	99.47	2.38
Hybrid Models	MISSFormer (Huang et al., 2021)	86.74	78.00	86.98	88.76	99.50	2.12
	Trans-Unet* (Chen et al., 2021)	87.28	78.86	87.09	89.84	99.52	2.20
	HiFormer-Base* (Heidari et al., 2023)	87.42	78.81	85.93	91.02	99.50	2.21
	H2Former* (He et al., 2023a)	87.59	79.22	87.61	89.75	99.53	2.02
	BEFUnet* (Manzari et al., 2024)	84.61	75.24	88.81	83.38	99.44	2.63
	CFFormer* (Ours)	88.18	80.08	87.50	90.84	99.53	1.89

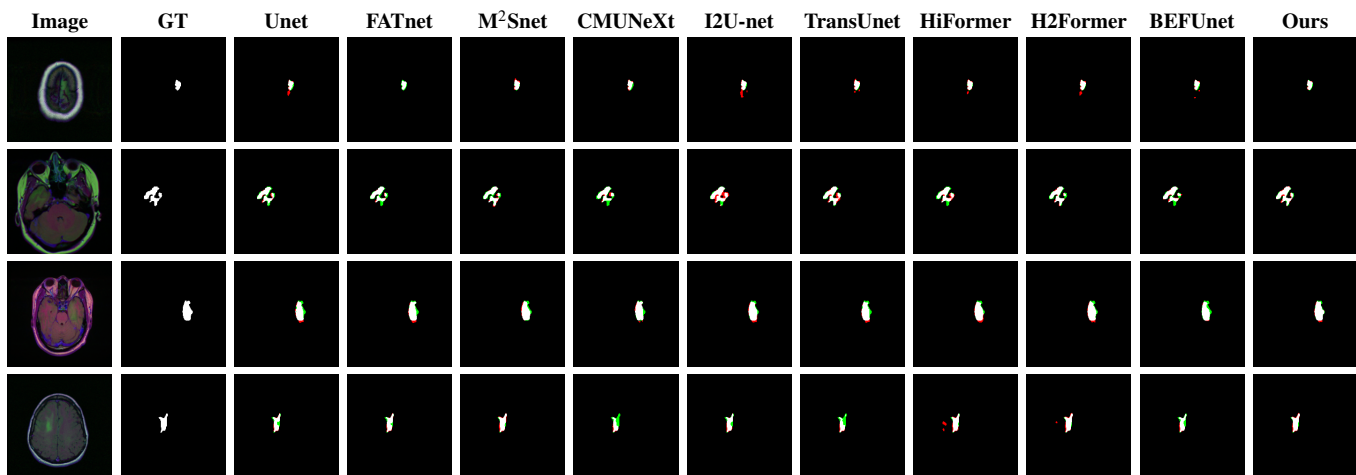


Fig. 8: Visualisation of Brain Tumor MRI datasets. Red represents over-segmentation, green under-segmentation, and white correct segmentation.

2023a) by 3.57%. In terms of the Jaccard index, our model exceeds HiFormer-Base (Heidari et al., 2023) by 0.86%. Our model also outperforms the state-of-the-art in pixel accuracy and HD95, achieving 99.53 and 1.89, respectively. Our model’s precision and recall are also highly competitive compared to other state-of-the-art models.

4.9. Ablation Study

In the ablation experiments, we first evaluate the combination of a CNN encoder and decoder, where the CNN employs ResNet34 (He et al., 2016) as the backbone to assess its segmentation performance on these datasets. Additionally, we test the performance of Swin Transformer V2 (Liu et al., 2022) as an encoder paired with our decoder. The results show that the CNN outperforms the Transformer on the ultrasound dataset, whereas the Transformer demonstrates superior performance on the polyp segmentation task.

Next, we experiment with dual encoders, using a simple convolution layer to fuse the feature maps. However, the results indicate that this approach performs worse than using a single encoder. This finding highlights the significant differences be-

tween CNNs and Transformers in spatial and channel features, which cannot be effectively eliminated with a simple convolutional operation.

To address the differences in channel features, especially when the number of feature maps is inconsistent, we introduce a selection mechanism to filter and map the features. Specifically, we construct a matrix to map the channel features based on the characteristics of the two encoders. In our architecture, the CNN features are fused with the channel-mapped Transformer features as input for the next CNN layer. Similarly, the Transformer features are fused with the channel-selected CNN features as input for the next Transformer layer. This approach enables the CNN to acquire global features with a larger receptive field, while providing the Transformer with more detailed local features.

Furthermore, we integrate the XFF module into the model to effectively fuse spatial features. Through iterative convolution operations and feature fusion, we gradually mitigate the significant differences in spatial features. As shown in Table 7, our model achieves notable improvements in both Dice and Jaccard metrics, with highly competitive performance on the

Table 7: Ablation study on the BUSI, Dataset B, CVC-ClinicDB, and Kvasir SEG datasets. The CNN employs ResNet34 (He et al., 2016) as the backbone, while the Transformer utilizes Swin Transformer V2 (Liu et al., 2022). **Red** indicates the best results, **Blue** is the second-best.

Model	BUSI			Kvasir SEG			Dataset B			CVC-ClinicDB		
	Dice↑	Jaccard↑	HD95↓	Dice↑	Jaccard↑	HD95↓	Dice↑	Jaccard↑	HD95↓	Dice↑	Jaccard↑	HD95↓
CNN + Decoder	84.59	75.80	8.17	88.97	85.89	9.83	85.31	77.53	7.64	92.44	87.37	1.20
Transformer + Decoder	82.75	74.09	10.72	90.83	84.64	8.33	83.81	76.47	11.43	93.24	87.93	2.37
CNN + Transformer + Decoder	84.71	76.29	7.41	90.39	84.30	7.66	82.97	74.42	10.69	92.48	87.47	1.22
CNN + Transformer + CFCA + XFF + Decoder	86.23	77.87	7.48	91.93	86.25	5.73	87.94	79.24	3.47	93.86	88.71	1.77

HD95 metric. These results strongly validate the effectiveness of the proposed CFCA and XFF modules.

4.10. Computational Performance Analysis

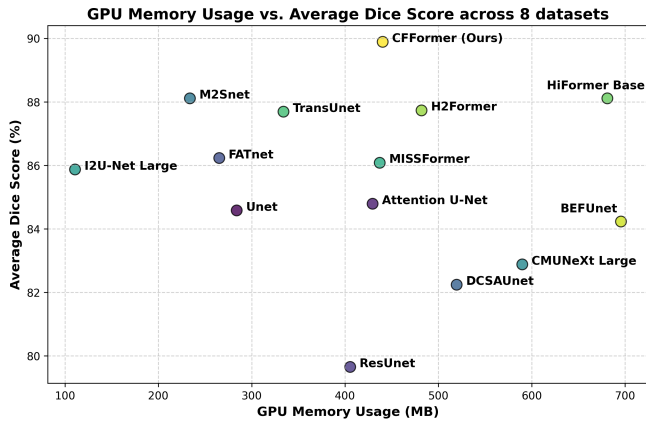


Fig. 9: An overview of GPU memory usage and the average Dice score across 8 datasets.

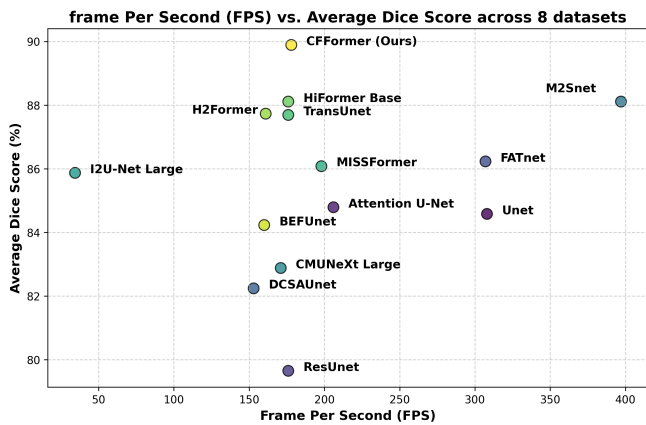


Fig. 10: An overview of FPS and the average Dice score across 8 datasets.

The parameter count alone is insufficient to capture the actual computational load of a model on a GPU. Consequently, we utilize peak GPU memory usage to provide a more holistic view of GPU resource consumption. Likewise, while Floating Point Operations per Second (FPS) offer a measure of computational complexity, they do not reliably reflect the model’s real-world inference performance. For a more accurate assessment, we report FPS to represent the inference speed directly.

As illustrated in Fig. 9, our model maintains a moderate GPU usage level, achieving substantially lower memory require-

ments than HiFormer-Base (Heidari et al., 2023), CMUNeXt-Large (Tang et al., 2024), DCSAUnet (Xu et al., 2023), BEFUnet (Manzari et al., 2024), and H2Former (He et al., 2023a). Despite this lower memory footprint, our model attains the highest average Dice score across the eight datasets compared with other SOTA models, highlighting its efficiency in resource utilization without compromising segmentation accuracy. In Fig. 10, we further observe our model’s average inference speed across 1600 images, where it outperforms several hybrid models, including H2Former (He et al., 2023a), HiFormer-Base (Heidari et al., 2023), TransUnet (Chen et al., 2021), BEFUnet (Manzari et al., 2024), as well as CNN-based models such as I2U-Net-Large (Dai et al., 2024), DCSAUnet (Xu et al., 2023), ResUnet (Diakogiannis et al., 2020) and CMUNeXt-Large (Tang et al., 2024). Remarkably, this speed advantage is coupled with the highest average Dice score across models, underscoring both the segmentation efficacy and inference efficiency of our approach. These findings suggest that our model strikes an optimal balance between GPU efficiency and competitive segmentation performance.

5. Conclusion

This paper proposes a novel hybrid CNN-Transformer architecture that effectively addresses the limitations of CNNs and Transformers in segmentation tasks. We introduce a Cross Feature Channel Attention (CFCA) module, which leverages lightweight cross-channel attention mechanisms between CNN and Transformer layers to map feature interactions, thereby enhancing the model’s expressive capacity. This module facilitates the integration of local features into the Transformer while ensuring that the CNN retains access to global feature information. Furthermore, we propose an X-Spatial Feature Fusion (XFF) module that efficiently fuses local and global features twice, providing a crucial output for skip connections. This design significantly improves the model’s ability to fuse semantic information and model contextual information. Extensive experiments across eight datasets and five modalities demonstrate the robust segmentation performance and strong generalization capability of our model.

Declaration of competing interest

The author declares that there are no financial interests or personal relationships related to this article that could influence the results and conclusions of the study.

Data Availability

All the data used in this study are obtained from publicly accessible datasets, and the code will be made available on GitHub.

Acknowledgments

This work is partially supported by the NSFC project (UNNC Project ID B0166), and Yongjiang Technology Innovation Project (2022A-097-G).

References

- Al-Dhabyani, W., Gomaa, M., Khaled, H., Fahmy, A., 2020. Dataset of breast ultrasound images. *Data in brief* 28, 104863.
- Asgari Taghanaki, S., Abhishek, K., Cohen, J.P., Cohen-Adad, J., Hamarneh, G., 2021. Deep semantic segmentation of natural and medical images: a review. *Artificial Intelligence Review* 54, 137–178.
- Ates, G.C., Mohan, P., Celik, E., 2023. Dual cross-attention for medical image segmentation. *Engineering Applications of Artificial Intelligence* 126, 107139.
- Azad, R., Aghdam, E.K., Rauland, A., Jia, Y., Avval, A.H., Bozorgpour, A., Karimijafarbigloo, S., Cohen, J.P., Adeli, E., Merhof, D., 2024. Medical image segmentation review: The success of u-net. *IEEE Transactions on Pattern Analysis and Machine Intelligence*.
- Brown, T.B., 2020. Language models are few-shot learners. *arXiv preprint arXiv:2005.14165*.
- Buda, M., Saha, A., Mazurowski, M.A., 2019. Association of genomic subtypes of lower-grade gliomas with shape features automatically extracted by a deep learning algorithm. *Computers in biology and medicine* 109, 218–225.
- Chen, J., Lu, Y., Yu, Q., Luo, X., Adeli, E., Wang, Y., Lu, L., Yuille, A.L., Zhou, Y., 2021. Transunet: Transformers make strong encoders for medical image segmentation. *arXiv preprint arXiv:2102.04306*.
- Dai, D., Dong, C., Yan, Q., Sun, Y., Zhang, C., Li, Z., Xu, S., 2024. I2u-net: A dual-path u-net with rich information interaction for medical image segmentation. *Medical Image Analysis*, 103241.
- Devlin, J., 2018. Bert: Pre-training of deep bidirectional transformers for language understanding. *arXiv preprint arXiv:1810.04805*.
- Diakogiannis, F.I., Waldner, F., Caccetta, P., Wu, C., 2020. Resunet-a: A deep learning framework for remote segmentation of remotely sensed data. *ISPRS Journal of Photogrammetry and Remote Sensing* 162, 94–114.
- Dosovitskiy, A., 2020. An image is worth 16x16 words: Transformers for image recognition at scale. *arXiv preprint arXiv:2010.11929*.
- Feng, S., Zhao, H., Shi, F., Cheng, X., Wang, M., Ma, Y., Xiang, D., Zhu, W., Chen, X., 2020. Cpfnet: Context pyramid fusion network for medical image segmentation. *IEEE transactions on medical imaging* 39, 3008–3018.
- Gao, Y., Zhou, M., Metaxas, D.N., 2021. Utmet: a hybrid transformer architecture for medical image segmentation, in: *Medical Image Computing and Computer Assisted Intervention–MICCAI 2021: 24th International Conference, Strasbourg, France, September 27–October 1, 2021, Proceedings, Part III* 24, Springer. pp. 61–71.
- Gutman, D., Codella, N.C., Celebi, E., Helba, B., Marchetti, M., Mishra, N., Halpern, A., 2016. Skin lesion analysis toward melanoma detection: A challenge at the international symposium on biomedical imaging (isbi) 2016, hosted by the international skin imaging collaboration (isic). *arXiv preprint arXiv:1605.01397*.
- Han, K., Wang, Y., Chen, H., Chen, X., Guo, J., Liu, Z., Tang, Y., Xiao, A., Xu, C., Xu, Y., et al., 2022. A survey on vision transformer. *IEEE transactions on pattern analysis and machine intelligence* 45, 87–110.
- He, A., Wang, K., Li, T., Du, C., Xia, S., Fu, H., 2023a. H2former: An efficient hierarchical hybrid transformer for medical image segmentation. *IEEE Transactions on Medical Imaging* 42, 2763–2775.
- He, K., Zhang, X., Ren, S., Sun, J., 2016. Deep residual learning for image recognition, in: *Proceedings of the IEEE conference on computer vision and pattern recognition*, pp. 770–778.
- He, Q., Yang, Q., Xie, M., 2023b. Hctnet: A hybrid cnn-transformer network for breast ultrasound image segmentation. *Computers in Biology and Medicine* 155, 106629.
- Heidari, M., Kazerouni, A., Soltany, M., Azad, R., Aghdam, E.K., Cohen-Adad, J., Merhof, D., 2023. Hiformer: Hierarchical multi-scale representations using transformers for medical image segmentation, in: *Proceedings of the IEEE/CVF winter conference on applications of computer vision*, pp. 6202–6212.
- Hu, J., Shen, L., Sun, G., 2018. Squeeze-and-excitation networks, in: *Proceedings of the IEEE conference on computer vision and pattern recognition*, pp. 7132–7141.
- Huang, X., Deng, Z., Li, D., Yuan, X., 2021. Missformer: An effective medical image segmentation transformer. *arXiv preprint arXiv:2109.07162*.
- Jégou, S., Drozdal, M., Vazquez, D., Romero, A., Bengio, Y., 2017. The one hundred layers tiramisu: Fully convolutional densenets for semantic segmentation, in: *Proceedings of the IEEE conference on computer vision and pattern recognition workshops*, pp. 11–19.
- Jha, D., Smedsrud, P.H., Riegler, M.A., Halvorsen, P., De Lange, T., Johansen, D., Johansen, H.D., 2020. Kvasir-seg: A segmented polyp dataset, in: *MultiMedia modeling: 26th international conference, MMM 2020, Daejeon, South Korea, January 5–8, 2020, proceedings, part II* 26, Springer. pp. 451–462.
- Jha, D., Smedsrud, P.H., Riegler, M.A., Johansen, D., De Lange, T., Halvorsen, P., Johansen, H.D., 2019. Resunet++: An advanced architecture for medical image segmentation, in: *2019 IEEE international symposium on multimedia (ISM)*, IEEE. pp. 225–2255.
- Kolda, T.G., Bader, B.W., 2009. Tensor decompositions and applications. *SIAM review* 51, 455–500.
- Landman, B., Xu, Z., Igelsias, J., Styner, M., Langerak, T., Klein, A., 2015. Miccai multi-atlas labeling beyond the cranial vault—workshop and challenge, in: *Proc. MICCAI Multi-Atlas Labeling Beyond Cranial Vault—Workshop Challenge*, p. 12.
- Li, X., Wang, W., Hu, X., Yang, J., 2019. Selective kernel networks, in: *Proceedings of the IEEE/CVF conference on computer vision and pattern recognition*, pp. 510–519.
- Li, Z., Li, D., Xu, C., Wang, W., Hong, Q., Li, Q., Tian, J., 2022. Tfncs: A cnn-transformer hybrid network for medical image segmentation, in: *International Conference on Artificial Neural Networks*, Springer. pp. 781–792.
- Liu, Z., Hu, H., Lin, Y., Yao, Z., Xie, Z., Wei, Y., Ning, J., Cao, Y., Zhang, Z., Dong, L., et al., 2022. Swin transformer v2: Scaling up capacity and resolution, in: *Proceedings of the IEEE/CVF conference on computer vision and pattern recognition*, pp. 12009–12019.
- Liu, Z., Lin, Y., Cao, Y., Hu, H., Wei, Y., Zhang, Z., Lin, S., Guo, B., 2021. Swin transformer: Hierarchical vision transformer using shifted windows, in: *Proceedings of the IEEE/CVF international conference on computer vision*, pp. 10012–10022.
- Liu, Z., Lv, Q., Yang, Z., Li, Y., Lee, C.H., Shen, L., 2023. Recent progress in transformer-based medical image analysis. *Computers in Biology and Medicine*, 107268.
- Manzari, O.N., Kaleybar, J.M., Saadat, H., Maleki, S., 2024. Befunet: A hybrid cnn-transformer architecture for precise medical image segmentation. *arXiv preprint arXiv:2402.08793*.
- Mendonça, T., Ferreira, P.M., Marques, J.S., Marcal, A.R., Rozeira, J., 2013. Ph 2-a dermoscopic image database for research and benchmarking, in: *2013 35th annual international conference of the IEEE engineering in medicine and biology society (EMBC)*, IEEE. pp. 5437–5440.
- Oktao, O., Schlemper, J., Folgoc, L.L., Lee, M., Heinrich, M., Misawa, K., Mori, K., McDonagh, S., Hammerla, N.Y., Kainz, B., et al., 2018. Attention u-net: Learning where to look for the pancreas. *arXiv preprint arXiv:1804.03999*.
- Ronneberger, O., Fischer, P., Brox, T., 2015. U-net: Convolutional networks for biomedical image segmentation, in: *Medical image computing and computer-assisted intervention–MICCAI 2015: 18th international conference, Munich, Germany, October 5–9, 2015, proceedings, part III* 18, Springer. pp. 234–241.
- Tang, F., Ding, J., Quan, Q., Wang, L., Ning, C., Zhou, S.K., 2024. Cmunext: An efficient medical image segmentation network based on large kernel and skip fusion, in: *2024 IEEE International Symposium on Biomedical Imaging (ISBI)*, IEEE. pp. 1–5.
- Wang, Q., Wu, B., Zhu, P., Li, P., Zuo, W., Hu, Q., 2020. Eca-net: Efficient channel attention for deep convolutional neural networks, in: *Proceedings of the IEEE/CVF conference on computer vision and pattern recognition*, pp.

11534–11542.

- Wang, Z., Zou, Y., Liu, P.X., 2021. Hybrid dilation and attention residual u-net for medical image segmentation. *Computers in biology and medicine* 134, 104449.
- Wu, H., Chen, S., Chen, G., Wang, W., Lei, B., Wen, Z., 2022. Fat-net: Feature adaptive transformers for automated skin lesion segmentation. *Medical image analysis* 76, 102327.
- Xu, Q., Ma, Z., Na, H., Duan, W., 2023. Dcsau-net: A deeper and more compact split-attention u-net for medical image segmentation. *Computers in Biology and Medicine* 154, 106626.
- Yao, W., Bai, J., Liao, W., Chen, Y., Liu, M., Xie, Y., 2024. From cnn to transformer: A review of medical image segmentation models. *Journal of Imaging Informatics in Medicine* , 1–19.
- Yap, M.H., Pons, G., Marti, J., Ganau, S., Sentis, M., Zwiggelaar, R., Davison, A.K., Marti, R., 2017. Automated breast ultrasound lesions detection using convolutional neural networks. *IEEE journal of biomedical and health informatics* 22, 1218–1226.
- Yuan, F., Zhang, Z., Fang, Z., 2023. An effective cnn and transformer complementary network for medical image segmentation. *Pattern Recognition* 136, 109228.
- Zhan, S., Yuan, Q., Lei, X., Huang, R., Guo, L., Liu, K., Chen, R., 2024. Bfnet: a full-encoder skip connect way for medical image segmentation. *Frontiers in Physiology* 15, 1412985.
- Zhang, H., Lian, J., Yi, Z., Wu, R., Lu, X., Ma, P., Ma, Y., 2024. Hau-net: Hybrid cnn-transformer for breast ultrasound image segmentation. *Biomedical Signal Processing and Control* 87, 105427.
- Zhang, Y., Liu, H., Hu, Q., 2021. Transfuse: Fusing transformers and cnns for medical image segmentation, in: *Medical Image Computing and Computer Assisted Intervention–MICCAI 2021*, Springer. pp. 14–24.
- Zhao, X., Jia, H., Pang, Y., Lv, L., Tian, F., Zhang, L., Sun, W., Lu, H., 2023. M^2 snet: Multi-scale in multi-scale subtraction network for medical image segmentation. *arXiv preprint arXiv:2303.10894* .
- Zhou, Z., Siddiquee, M.M.R., Tajbakhsh, N., Liang, J., 2019. Unet++: Redesigning skip connections to exploit multiscale features in image segmentation. *IEEE transactions on medical imaging* 39, 1856–1867.